ACS SENSORS

pubs.acs.org/acssensors

Article

Real-Time Monitoring of Biomolecules: Dynamic Response Limits of Affinity-Based Sensors

Rafiq M. Lubken, Arthur M. de Jong, and Menno W. J. Prins*

Cite This: *ACS Sens.* 2022, 7, 286−295

Read Online

ACCESS | Metrics & More | Article Recommendations | Supporting Information

ABSTRACT: Sensors for monitoring biomolecular dynamics in biological systems and biotechnological processes in real time, need to accurately and precisely reconstruct concentration−time profiles. This requirement becomes challenging when transport processes and biochemical kinetics are important, as is typically the case for biomarkers at low concentrations. Here, we present a comprehensive methodology to study the concentration−time profiles generated by affinity-based sensors that continuously interact with a biological system of interest. Simulations are performed for sensors with diffusion-based sampling (*e.g.*, a sensor patch on the skin) and advection-based sampling (*e.g.*, a sensor connected to a catheter). The simulations clarify how transport processes and molecular binding kinetics result in concentration gradients and time delays in the sensor system. Using these simulations, measured and true concentration−time profiles of insulin were compared as a function of sensor design parameters. The results lead to guidelines on how biomolecular monitoring sensors can be designed for optimal bioanalytical performance in terms of concentration and time properties.

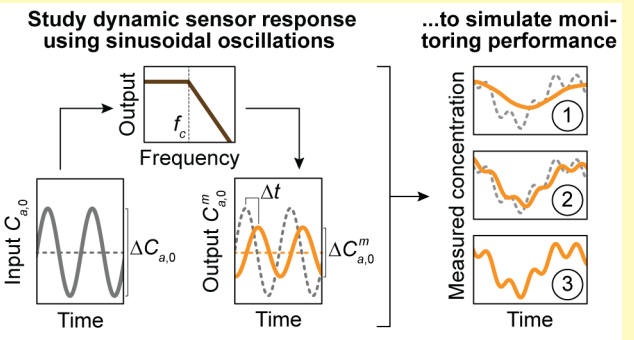

KEYWORDS: *monitoring, sensing, sensor performance, concentration change, lag time, biomolecules, affinity kinetics*

Biological systems and biotechnological processes exhibit time dependencies that are imposed by dynamic changes of constituting biomolecules, such as nutrients, hormones, proteins, and nucleic acids. To study dynamic processes in real time, monitoring sensors that can reveal biomolecular concentration−time profiles are needed, to support fundamental research,[1−7] patient monitoring,[8−14] and closed-loop control applications.[15−22] Such monitoring sensors should be able to reconstruct concentration−time profiles accurately and precisely, in both concentration and time, and the sensors should be suitable for measuring a wide variety of molecular markers.

The developments in biomolecular monitoring have mainly focused on measuring high-concentration metabolites, such as glucose and lactate.[8,12,13] Due to their small size and high concentrations, the transport and detection of these biomolecules is fast. However, in the case of biomolecular markers at lower concentrations, fewer molecules are available and transport limitations become important.[22] Furthermore, biochemical reactions are slow at low concentrations,[23] generating time delays in the sensors and time-related errors in the concentration results.

To understand and predict how real-time monitoring of biomolecules is limited by dynamic processes, we present a comprehensive methodology for studying affinity-based sensors that continuously interact with a time-dependent system of interest. Here, concentration changes, which are present in a system of interest, propagate into a monitoring sensor by diffusion-based sampling or advection-based sampling. We focus on sensing by biochemical affinity between binder molecules and analyte molecules since this is a very generic molecular mechanism for achieving specific and sensitive measurements. Frequency-dependent simulations are presented to clarify how concentration gradients and time delays are caused by mass transport processes and molecular binding kinetics. The results lead to relationships between sensor design parameters and measurable concentration change rates, time delays, and concentration errors. This will help researchers to design biomolecular sensors for optimal bioanalytical performance in terms of concentration and time properties.

BIOMOLECULAR MONITORING WITH CONTINUOUS ANALYTE EXCHANGE

The conceptual layout of the monitoring arrangement is sketched in Figure 1. Figure 1a shows continuous analyte

Received: November 1, 2021
Accepted: December 9, 2021
Published: January 3, 2022

https://doi.org/10.1021/acssensors.1c02307
ACS Sens. 2022, 7, 286−295

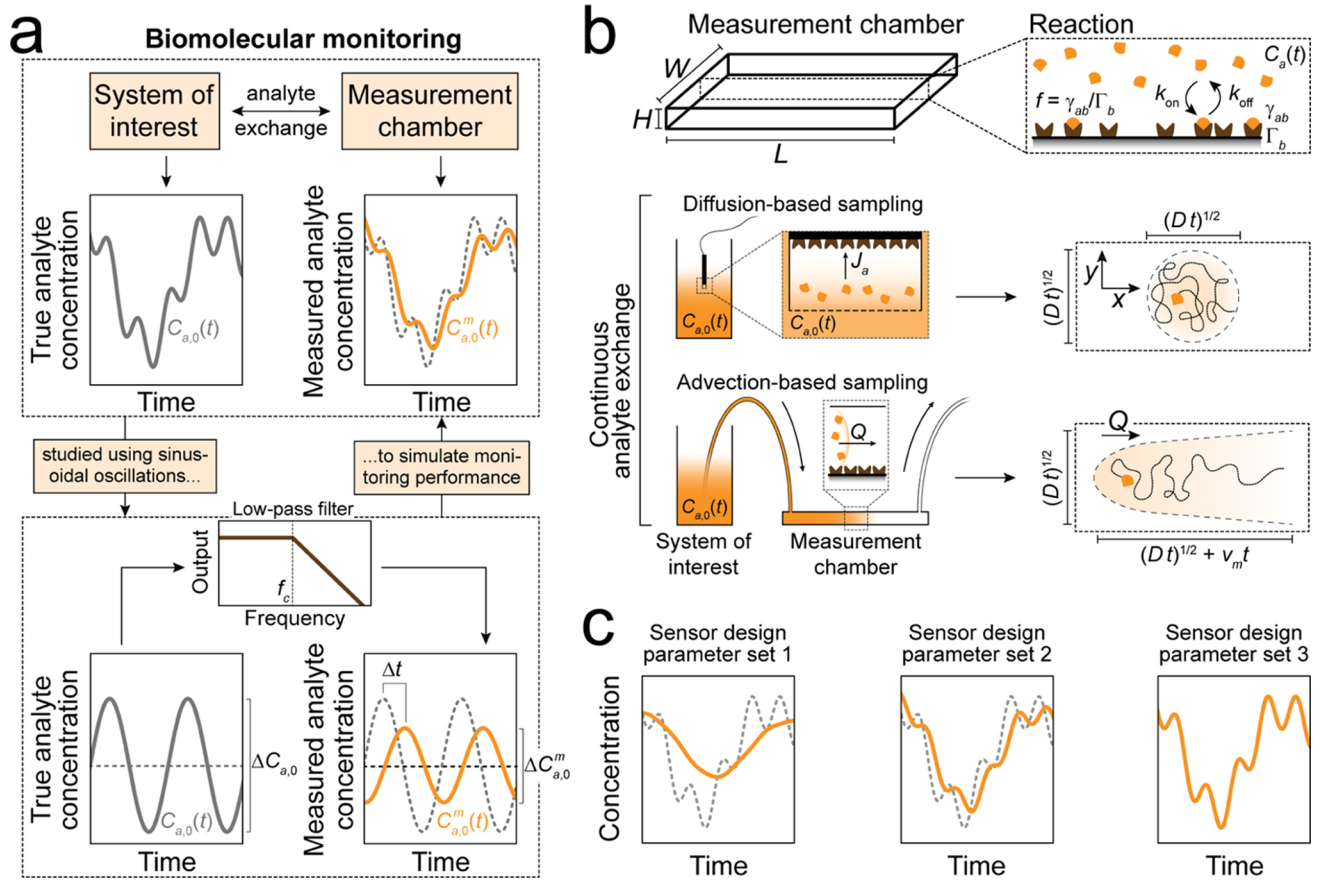

Figure 1. Conceptual layout of a biomolecular monitoring system with continuous analyte exchange. (a) Biomolecular monitoring system with continuous analyte exchange between a system of interest and a measurement chamber, where the system of interest exhibits a dynamic concentration−time profile $C_{a,0}(t)$ (gray line), which results in a measured concentration−time profile $C^{m}_{a,0}(t)$ (orange line). Ideally, the measured concentration−time profile closely resembles the true concentration−time profile (dashed line *vs* solid line). The monitoring system can be mimicked by a low-pass filter with a cutoff frequency f_c. The system of interest supplies an oscillating concentration−time profile $C_{a,0}(t)$ with concentration change $\Delta C_{a,0}$, which leads to a measured concentration $C^{m}_{a,0}(t)$ with concentration change $\Delta C^{m}_{a,0}$. A comparison of the true and measured concentration−time profiles (dashed line *vs* solid line) gives the system response in terms of the concentration change ratios and lag time Δt. (b) Geometry of the measurement chamber with height H, width W, and length L. The signal of the sensor is generated by an affinity reaction at the sensor surface, where analyte molecules (orange) associate with and dissociate from binder molecules (brown), of which the reaction rates are described by the association rate constant k_{on}, the dissociation rate constant k_{off}, the binder density Γ_b, the concentration−time profile $C_a(t)$ at the sensor surface, and the analyte−binder complex density γ_{ab}. Two modes of continuous analyte exchange are studied: analyte exchange by diffusion (top) and by advection (bottom). In the measurement chamber, mass transport by diffusion occurs in both x- and y-direction, caused by a concentration gradient (orange gradient) that results in a net molecular flux J_a, which scales with the diffusion coefficient D. Mass transport by advection occurs in the x-direction only, caused by a flow with mean flow velocity v_m and flow rate Q. (c) Examples of how the sensor performance can differ for different sensor design parameter sets.

exchange between a biological or biotechnological system of interest and a measurement chamber. The system of interest exhibits dynamic changes of analyte concentration where the sensing aim is to achieve minimal differences between the true concentration−time profile $C_{a,0}(t)$ and the measured concentration−time profile $C^{m}_{a,0}(t)$. The basic modeling approach is to study analyte concentrations that vary with a sinusoidal time dependence around a mean concentration value

$$C(t) = C + \frac{\Delta C}{2}\sin(2\pi ft + \phi) \quad (1)$$

with $C(t)$ being the oscillating concentration−time profile, C the mean concentration, ΔC the top-to-top amplitude of concentration change, f the oscillation frequency, and ϕ the phase. In the analysis, the concentration change ΔC is a small perturbation on the mean value C (a few percent). The advantage of studying sinusoidal functions is that concentration−time profiles of arbitrary shape can be reconstructed by frequency decomposition, as will be discussed later in this paper. Concentration symbols with subscript "a" refer to analyte concentrations: the analyte concentration−time profile in the system of interest is denoted by $C_{a,0}(t)$, at the sensor surface by $C_a(t)$, and the measured analyte concentration−time profile by $C^{m}_{a,0}(t)$. From the simulations in this paper, it will become apparent that the response of the monitoring system resembles a low-pass filter: at low frequencies, the measured and true concentration−time profiles are close to each other; however, at frequencies higher than a cutoff frequency f_c, the measured concentration−time profile deviates from the true concentration−time profile, visible in the concentration change ΔC and in the lag time Δt that corresponds to the phase lag ϕ.

The measurement chamber is assumed to be rectangular with height H, width W, and length L (see Figure 1b). The bottom surface of the measurement chamber is a sensor

https://doi.org/10.1021/acssensors.1c02307
ACS Sens. 2022, 7, 286−295

surface with affinity binder molecules (brown), where association and dissociation occur of the analyte molecules (orange). The association and dissociation rates depend on the association rate constant k_{on}, the dissociation rate constant k_{off}, the binder surface density Γ_b, the analyte concentration−time profile $C_a(t)$ at the sensor surface, and the surface density of analyte−binder complexes γ_{ab}. The binding of analyte molecules to binder molecules on the sensor surface causes γ_{ab} to change as a function of time, resulting in a time-dependent signal, which relates to the oscillating analyte concentration $C_{a,0}(t)$ in the system of interest (see Supplementary Note 1).

We study two modes of continuous analyte exchange, namely, analyte exchange by diffusion only (top sketch) and analyte exchange by advection as well as diffusion (bottom sketch). Diffusion-based sampling applies to a sensor that is worn on the skin or that is fully embedded in a bioreactor, for example.[8−10] Advection-based sampling applies to a sensor that is connected to a patient via a catheter or that is connected to a bioreactor via a sampling line.[19−21] In the case of diffusion-based sampling, a net molecular flux J_a is caused by a concentration difference (orange gradient), facilitating mass transport between the system of interest and the measurement chamber. In the case of advection-based sampling, a laminar flow with flow rate Q facilitates mass transport between the system of interest and the measurement chamber. In the simulations, it is assumed that diffusion occurs in both the longitudinal (x-direction) and lateral directions (y-direction) and scales with the diffusion coefficient D. In the case of advective exchange, the diffusive transport is superposed onto the advective transport caused by a flow, of which the transport scales with the mean flow velocity v_m and thus the flow rate Q. In this paper, different design parameters will be studied, which lead to different sensor performances, as exemplified in Figure 1c.

Biomolecular monitoring applications differ widely in the analyte molecules that need to be measured, their concentrations, and their concentration change rates. Figure 2 sketches an overview of analyte concentrations in blood (in M) and typical concentration change rates (CCRs, in M h^{-1}) for biomedical monitoring applications such as diabetes (glucose and insulin),[12,13] organ failure (*e.g.*, creatinine),[24,25] and inflammation (*e.g.*, CRP, PCT, cytokines).[1−3,26,27] The CCRs were calculated by estimating characteristic concentration changes $\Delta C_{a,0}$ and typical fluctuation times t_{fluc} (see Supplementary Note 2). For example, blood glucose concentrations vary between 4 and 8 mM in healthy persons, while for diabetic patients, the glucose level can increase to 10−15 mM and higher within a period of $t_{fluc} \sim 30$ min. This results in a typical maximum CCR of about 20 mM h^{-1}. At the low end of the concentration scale, cytokine biomarker interleukin-6 (IL-6) is indicated. Physiological IL-6 concentrations are below 0.5 pM, while for patients with acute inflammatory stress, *e.g.*, due to sepsis or due to cytokine release syndrome, the IL-6 concentration can increase to 10−100 pM and higher within a period of a few hours ($t_{fluc} \sim 2$ h). This results in a typical maximum CCR of about 30 pM h^{-1}.

In this paper, the dynamic response of sensors with different designs is characterized by two parameters: first, the lag time Δt of the sensor signal with respect to the input concentration (see Figure 1), and second, the *rate sensitivity*, *i.e.*, the minimum CCR that can be measured with an error of 10% (see Supplementary Note 5). We refer to this minimum CCR as the limit of quantification of CCR (LoCCR). In the next sections, we study how design parameters influence the lag time and rate sensitivity using standard parameter values as listed in Table 1. The sensor signal and its time characteristics are quantified by finite-element simulations to investigate the consequences of mass transport and reactions at the sensor surface. The rate sensitivity is quantified by calculating the stochastic variabilities in the number of analyte−binder complexes, for concentration−time profiles with varying concentration levels and CCRs.

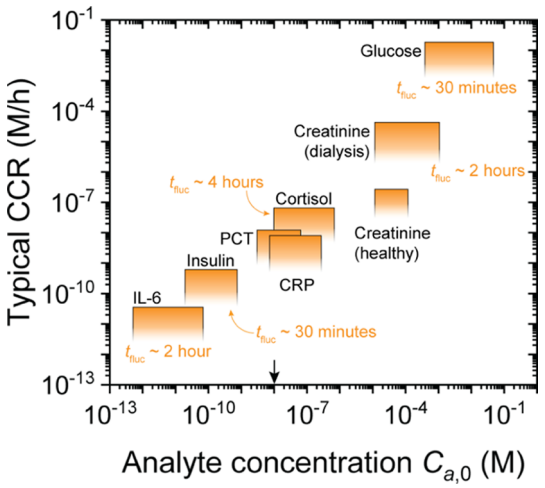

Figure 2. Typical concentration change rates (CCRs) and mean analyte concentrations $C_{a,0}$ for various analyte molecules in blood plasma. CCRs were calculated by estimating a characteristic concentration change $\Delta C_{a,0}$ and a corresponding characteristic fluctuation time t_{fluc} (see Supplementary Note 2) based on reported concentration−time profiles in blood plasma. Abbreviations: IL-6 (interleukin-6), PCT (procalcitonin), and CRP (C-reactive protein). The black arrow indicates the standard parameter value for the mean analyte concentration $C_{a,0}$ as listed in Table 1.

EXPERIMENTAL SECTION

Finite-Element Analysis. Finite-element simulations were performed by solving diffusion, advection and reaction equations simultaneously using COMSOL (COMSOL Multiphysics 5.5) and MATLAB (MATLAB R2019a, COMSOL Multiphysics LiveLink for MATLAB) (see Supplementary Note 1). The LoCCR was reported at a distance $L/2$ in the measurement chamber (Figure 1b), where the signal was collected over a signal collection area A_s = 1 mm^2 with a binder molecule density $\Gamma_b = 10^{-9}$ mol m^{-2} (see Supplementary Note 5).

Frequency Analysis. The amplitude and the phase lag of the concentration at the sensor surface (Figures 3a and 4a,b), analyte−binder complex density (Figure 3b), and the measured concentration (Figures 3c and 4c) were calculated using the Fourier transform of its concentration/density profile. The calculated values were compared to the amplitude and the phase (*i.e.*, $\phi = 0$) of the input profile. The cutoff frequency was determined at the frequency where the observed amplitude was 50% of the input amplitude. The LoCCR was determined according to Supplementary Notes 2 and 5.

RESULTS AND DISCUSSION

Response of a Monitoring System with Diffusion-Based Sampling. First, we consider the case where the transport of analyte molecules between a system of interest and a sensor measurement chamber is governed by diffusion only. Figure 3 shows how the analyte concentration at the sensor surface and the analyte−binder complex density respond to an

https://doi.org/10.1021/acssensors.1c02307
ACS Sens. 2022, 7, 286−295

Table 1. Standard Parameter Values Used in the Finite-Element Simulations[a]

	parameter	value	description
input	H	100 μm	measurement chamber height
	L	1 cm	measurement chamber length
	W	2 mm	measurement chamber width
	D	10^{-10} m^2 s^{-1}	diffusion coefficient of the analyte molecule
	Q	120 μL min^{-1}	flow rate
	k_{off}	10^{-2} s^{-1}	dissociation rate constant
	k_{on}	10^{6} M^{-1} s^{-1}	association rate constant
	$C_{a,0}$	10 nM	mean analyte concentration in the system of interest
derived	$\lambda = L/H$	100	aspect ratio of measurement chamber
	$\tau_D = H^2/D$	100 s	characteristic diffusion time
	$\tau_A = HLW/Q$	1 s	characteristic advection time
	$\tau_R = (k_{on}C_{a,0} + k_{off})^{-1}$	50 s	characteristic reaction time
	$K_d = k_{off}/k_{on}$	10 nM	equilibrium dissociation constant
	$\Delta C_{a,0}/C_{a,0}$	0.05 (5%)	relative concentration change
	$Da = \frac{\tau_D}{\tau_R} = \frac{(k_{on}C_{a,0} + k_{off})H^2}{D}$	2	Damköhler number
	$Pe_L = \frac{\tau_D}{\tau_A} = \frac{Q}{\lambda DW}$	100	longitudinal Péclet number

[a]Details about the simulations are described in Supplementary Note 1.

oscillating concentration $C_{a,0}(t)$ in the system of interest, with concentration change $\Delta C_{a,0}$ for various oscillation frequencies (see Supplementary Note 2). Figure 3a shows how diffusive mass transport influences the concentration profile $C_a(t)$ at the sensor surface, by quantifying the concentration change ΔC_a at the sensor surface (top, orange line, normalized to $\Delta C_{a,0}$), and the lag time Δt (bottom, orange line, normalized to the diffusion time τ_D), given as a function of f (normalized to the diffusion time τ_D). In the top graph, for small f, the concentration change ratio $\Delta C_a/\Delta C_{a,0}$ is close to unity, indicating that the concentration change at the sensor surface is approximately equal to the concentration change in the system of interest. Since the oscillation time $1/f$ is larger than τ_D, the analyte molecules are evenly distributed throughout the measurement chamber, *i.e.*, there is no concentration gradient. For large f, $\Delta C_a/\Delta C_{a,0}$ decreases for increasing f, which means that the concentration change at the sensor surface is smaller than the concentration change in the system of interest. Since $1/f$ is now smaller than τ_D, a concentration gradient is present in the measurement chamber in the direction of H (see top sketch). This gradient results in dispersion of analyte molecules, which effectively reduces ΔC_a. A characteristic parameter to describe this decrease in $\Delta C_a/\Delta C_{a,0}$ is the cutoff frequency f_c, which is the frequency at which $\Delta C_a/\Delta C_{a,0} = 0.5$ (horizontal dotted black line). In this case, the diffusion-induced cutoff frequency f_c^D is equal to $f_c^D\tau_D \cong 0.65$ (vertical dotted black line). The bottom graph shows that for f smaller than f_c^D, the observed lag time Δt is independent of f, since within a period of $1/f$, analyte molecules can be transported throughout the measurement chamber by diffusion. This results in a homogeneous analyte concentration in the measurement chamber where Δt is only determined by diffusion ($\Delta t \sim \tau_D$). For f larger than f_c^D, a concentration gradient is present in the measurement chamber in the direction of H (see top sketch). Now Δt decreases according to $\Delta t \propto 1/\sqrt{f}$ (dashed black line, see Supplementary Note 3), concomitant with a reduction in ΔC_a (top graph). The inset shows the phase lag $\Delta\phi$ as a function of f. For increasing f, the absolute phase lag increases ($\Delta\phi$ becomes more negative) due to the time needed for the transport of analyte molecules from the top of the measurement chamber to the sensor surface. For a large f, the concentration at the sensor surface can lag multiple cycles ($\Delta\phi > 2\pi$) with respect to the concentration in the system of interest (not shown here).

Figure 3b shows how the association and dissociation of analyte molecules to binder molecules influence the measured signal. Mass transport effects are neglected and the concentration profile $C_a(t)$ at the sensor surface oscillates with a frequency f. The top graph shows the change in analyte–binder complex density $\Delta\gamma_{ab}$, normalized to the expected analyte–binder complex density change $\Delta\gamma_{ab}^{exp}$ based on the concentration profile $C_a(t)$ at the sensor surface (see Supplementary Note 4). The bottom graph shows the lag time Δt as a function of the frequency f (normalized to the reaction time τ_R). For small f, $\Delta\gamma_{ab}/\Delta\gamma_{ab}^{exp}$ is close to unity, indicating that the affinity reaction reaches equilibrium since the oscillation time $1/f$ is larger than the reaction time τ_R (see Table 1). For a large f, $\Delta\gamma_{ab}/\Delta\gamma_{ab}^{exp}$ decreases, indicating that fewer analyte molecules bind to binder molecules on the sensor surface than expected based on $C_a(t)$ under equilibrium conditions. This results in a reaction-induced cutoff frequency f_c^R, at $f_c^R\tau_R \cong 0.27$ (vertical dotted black line). For f smaller than f_c^R, Δt is largely independent of f. Now equilibrium is reached, causing the lag time to be determined by the time to equilibrium, *i.e.*, Δt is reaction-limited ($\Delta t \sim \tau_R$). For f larger than f_c^R, Δt depends on f as $\Delta t \propto 1/f$ (dashed black line, see Supplementary Note 3). The inset shows the phase lag $\Delta\phi$ as a function of f. For increasing f, the absolute phase lag increases ($\Delta\phi$ becomes more negative) since fewer analyte–binder complexes are formed within a time $1/f$. For large f, the phase lag reaches a minimum value of $\Delta\phi = -\pi/2$ (horizontal black dotted line) with respect to γ_{ab}^{exp} since the reaction rates are directly related to the analyte concentration C_a at the sensor surface and therefore the phase lag cannot be more negative (see Supplementary Note 3).

Figure 3c shows the cutoff frequency f_c as a function of the measurement chamber height H (top) and the mean analyte concentration $C_{a,0}$ in the system of interest (bottom,

https://doi.org/10.1021/acssensors.1c02307
ACS Sens. 2022, 7, 286–295

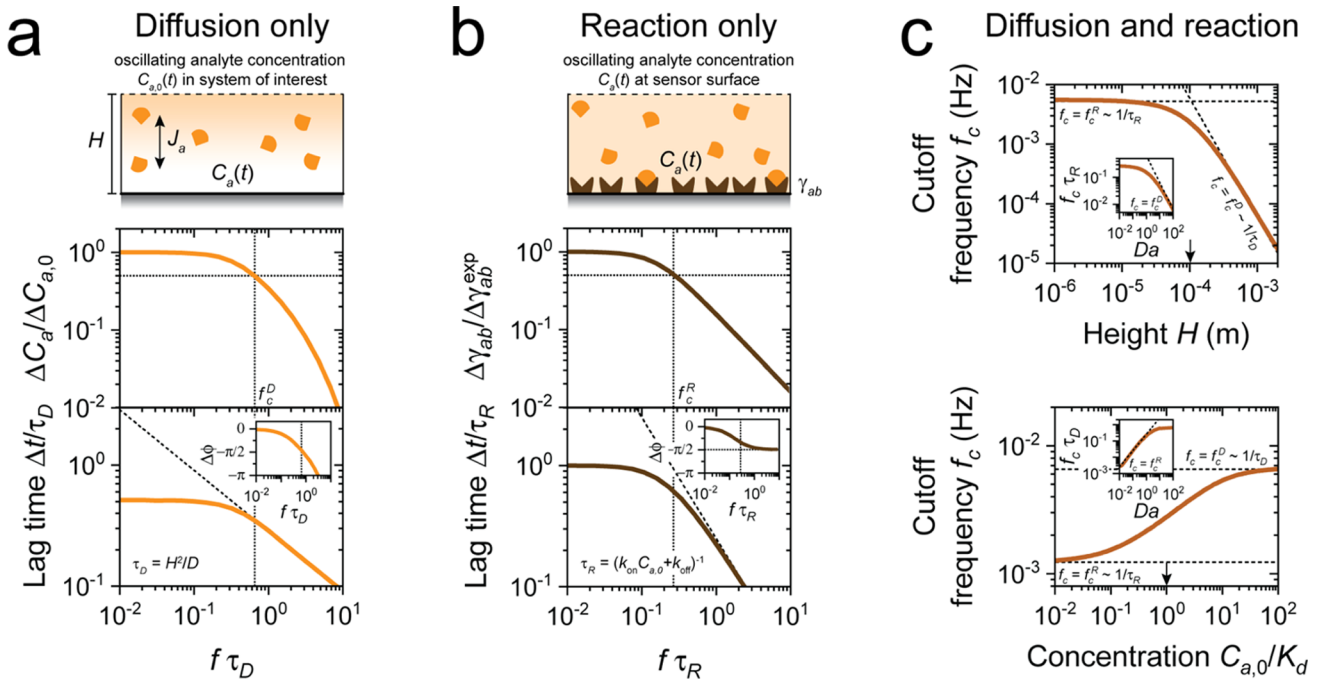

Figure 3. Response of a biomolecular monitoring system with continuous analyte exchange by diffusion-based sampling. (a) Frequency response when only diffusion is considered. Top graph: concentration change ΔC_a at the sensor surface (normalized to the concentration change $\Delta C_{a,0}$ in the system of interest) as a function of the frequency f (normalized to the diffusion time τ_D). The diffusion-induced cutoff frequency f_c^D (horizontal dotted black line) is $f_c^D\tau_D \cong 0.65$ (vertical dotted black line). Bottom graph: lag time Δt (normalized to the diffusion time τ_D) as a function of f (normalized to the diffusion time τ_D). For large f, Δt scales as $\Delta t \propto 1/\sqrt{f}$ (dashed black line, see Supplementary Note 3). The inset shows the phase lag $\Delta\phi$ as a function of f. The sketch above the graphs visualizes a measurement chamber with a concentration flux J_a caused by a concentration gradient (orange gradient). (b) Frequency response when only the surface reaction is considered. Top graph: analyte−binder complex density change $\Delta\gamma_{ab}$ (normalized to the expected analyte−binder complex density change $\Delta\gamma_{ab}^{exp}$, see Supplementary Note 4) as a function of f (normalized to the reaction time τ_R). The reaction-induced cutoff frequency f_c^R is $f_c^R\tau_D \cong 0.27$ (vertical dotted black line). Bottom graph: lag time Δt (normalized to the reaction time τ_R) as a function of f (normalized to the reaction time τ_R). For large f, Δt scales according to $\Delta t \propto 1/f$ (dashed black line, see Supplementary Note 3). The inset shows the phase lag $\Delta\phi$ as a function of f, where $\Delta\phi$ reaches a maximum negative value (see Supplementary Note 3). The sketch above the graphs visualizes a measurement chamber with an oscillating concentration $C_a(t)$ at the sensor surface and a resulting oscillating analyte−binder complex density γ_{ab}. (c) Cutoff frequency f_c as a function of measurement chamber height H (top) and mean analyte concentration $C_{a,0}$ in the system of interest (bottom). Top graph: for small H, f_c is reaction-limited, where $f_c = f_c^R \sim 1/\tau_R$, while for large H, f_c is diffusion-limited with $f_c = f_c^D \sim 1/\tau_D$. The inset shows f_c, normalized to the reaction time τ_R, as a function of the Damköhler number Da, with $f_c = f_c^D = \alpha_1/\tau_D$ and $\alpha_1 \cong 0.65$ (dashed black line, cf. panel a). Bottom graph: for low $C_{a,0}$, f_c is reaction-limited and $f_c = f_c^R \sim 1/\tau_R$, while for high $C_{a,0}$, f_c is diffusion-limited with $f_c = f_c^D \sim 1/\tau_D$. The inset shows f_c, normalized to the diffusion time τ_D, as a function of Da with $f_c = f_c^R = \alpha_2/\tau_D$ and $\alpha_2 \cong 0.27$ (dashed black line, cf. panel b). Note that using standard parameter values as listed in Table 1, the full range of Da cannot be reached by only changing $C_{a,0}$ because τ_R becomes dissociation rate-limited when $C_{a,0} \ll K_d$ (see Table 1); therefore, k_{off} was varied instead. The black arrows indicate standard parameter values as listed in Table 1.

normalized to the equilibrium dissociation constant K_d) when both diffusion and reaction processes are considered. Standard values for the chamber height H and mean concentration $C_{a,0}$ are indicated by the black arrows (see Table 1). For small H, the diffusion time τ_D is short since analyte molecules only need to travel a short distance from the top of the measurement chamber to the sensor surface. This causes the observed cutoff frequency f_c to be reaction-limited where $f_c = f_c^R \sim 1/\tau_R$. For large H, analyte molecules need to travel a long distance, which causes f_c to be diffusion-limited where $f_c = f_c^D \sim 1/\tau_D$. For small $C_{a,0}$, the reaction is slow since the reaction time τ_R is determined by the dissociation rate (see Table 1), causing f_c to be reaction-limited. For large $C_{a,0}$, τ_R is short since the reaction time τ_R is determined by the association rate, causing f_c to be diffusion-limited. The insets show f_c (normalized to the reaction time τ_R) as a function of the Damköhler number Da (see Table 1). Da is a dimensionless parameter describing the relative contribution of reaction and diffusion to the observed time scale (for $Da \gg 1$, diffusion is slow relative to reaction; for $Da \ll 1$, reaction is slow relative to diffusion). For a high Da, the cutoff frequency is diffusion-limited, while for a low Da, the cutoff frequency is reaction-limited.

Response of a Monitoring System with Advection-Based Sampling. Figure 4 shows how dynamic concentration changes generate signals in a monitoring sensor based on advective sampling, *i.e.*, sampling dominated by flow. Figure 4a visualizes how diffusion and advection jointly influence the concentration profile $C_a(t)$ at the sensor surface. The concentration change ΔC_a at the sensor surface (top, orange line, normalized to concentration change $\Delta C_{a,0}$ in the system of interest) and the lag time Δt (bottom, orange line, normalized to the advection time τ_A) are given as a function of the oscillation frequency f (normalized to τ_A) of the analyte concentration $C_{a,0}$ in the system of interest. Here, a longitudinal Péclet number $Pe_L = \tau_D/\tau_A = 100$ was assumed (see Table 1), where Pe_L describes the relative contribution of diffusion and advection to the transport process (for $Pe_L \gg 1$, diffusion is slow relative to advection; for $Pe_L \ll 1$, advection is slow relative to diffusion). In the top graph, for small f, $\Delta C_a/\Delta C_{a,0}$ equals unity, indicating that the concentration is evenly

https://doi.org/10.1021/acssensors.1c02307
ACS Sens. 2022, 7, 286−295

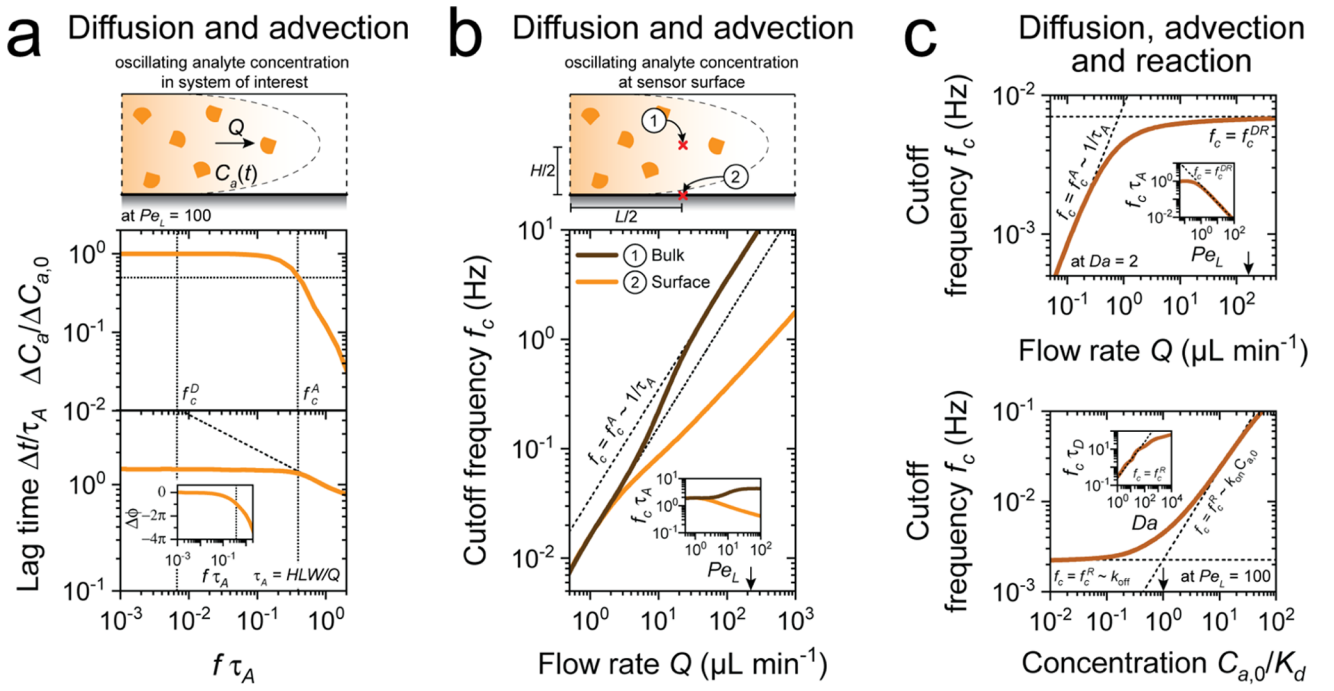

Figure 4. Response of a biomolecular monitoring system with continuous analyte exchange by advection-based sampling. (a) Frequency response when only diffusion and advection are considered, for an advection-dominated sensor geometry with Pe_L = 100 (see Table 1). Top graph: concentration change ΔC_a at the sensor surface, normalized to the concentration change $\Delta C_{a,0}$ in the system of interest, as a function of the frequency f (normalized to the advection time τ_A), measured at the sensor surface at distance $L/2$ from the inlet (see also the sketch in panel b). The diffusion-induced cutoff frequency f_c^D is taken from Figure 3a, and the advection-induced cutoff frequency f_c^A is found to be $f_c^A\tau_A \cong 0.39$ (vertical dotted black line) and roughly equals $f_c^A = 100{\cdot}f_c^D$. Bottom graph: lag time Δt, normalized to τ_A, as a function of the frequency f, normalized to τ_A. For large f, Δt scales according to $\Delta t \propto 1/\sqrt[3]{f}$ (black dashed line). (b) Cutoff frequency as a function of flow rate Q when only diffusion and advection are taken into account, measuring in the middle in the bulk of the measurement chamber at height $H/2$ (dark brown line) and at the sensor surface of the measurement chamber (orange line) both at distance $L/2$ from the inlet. For increasing Q, measuring in the bulk results in an advection-limited cutoff frequency (dashed black lines). The inset shows the same data with the observed cutoff frequency f_c, normalized to the advection time τ_A, as a function of the longitudinal Péclet number Pe_L. For small Pe_L, f_c for both bulk and surface measurements are comparable with $f_c = f_c^D$. For increasing Pe_L, f_c increases due to a higher flow rate, until the system becomes advection-limited. Measuring at the sensor surface results in a weaker dependency on τ_A than $1/\tau_A$. (c) Cutoff frequency f_c as a function of chamber height H with a fixed chamber length L (top) and mean analyte concentration $C_{a,0}$ in the system of interest (bottom) for a sensor when diffusion, advection, and reaction are taken into account. Top graph: for small H, f_c is reaction-limited where $f_c = f_c^R \sim 1/\tau_R$, while for large H, f_c is diffusion-limited with $f_c = f_c^D \sim 1/\tau_D$. The inset shows the same data with the cutoff frequency f_c, normalized to the reaction time τ_R, as a function of the Damköhler number. Bottom graph: for H = 100 μm (see Table 1), the cutoff frequency is reaction-limited (top graph). Therefore, for low $C_{a,0}$, f_c is dissociation rate-limited and $f_c = f_c^R \sim k_{off}$, while for high $C_{a,0}$, f_c is association rate-limited with $f_c = f_c^R \sim k_{on}C_{a,0}$. The inset shows the same data with the cutoff frequency f_c, normalized to the diffusion time τ_D, as a function of the Damköhler number. f_c becomes diffusion-limited at $Da \gg 1$ and reaches a plateau level larger than $f_c\tau_D = 1$ (cf. Figure 3c) since $\tau_D = H^2/D$, while the actual distance over which molecules decreases for increasing Q. Note that using the standard parameter values in Table 1, the full range of Da cannot be reached by only changing $C_{a,0}$ because τ_R becomes dissociation rate-limited when $C_{a,0} \ll K_d$ (see Table 1); therefore, k_{off} was varied instead. The black arrows indicate standard parameter values as listed in Table 1.

distributed throughout the measurement chamber. For a large f, $\Delta C_a/\Delta C_{a,0}$ decreases, which indicates a concentration gradient in the measurement chamber perpendicular to the velocity profile. This results in an advection-induced cutoff frequency f_c^A (horizontal dotted black line), which can be found at $f_c^A\tau_A \cong 0.39$ (vertical dotted black line). Note that the advection-induced cutoff frequency roughly equals $f_c^A = 100{\cdot}f_c^D$ since Pe_L = 100, where f_c^D is the cutoff frequency for a monitoring system with diffusion-based sampling (*cf.* Figure 3). In the bottom graph, for a small f, the observed lag time Δt of the concentration at the sensor surface compared to the concentration in the system of interest is largely independent of f since the analyte concentration is homogeneous in the measurement chamber, causing the lag time to be advection-limited ($\Delta t \sim \tau_A$). For f larger than f_c^A, a concentration gradient is present in the measurement chamber, causing a loss in ΔC_a due to dispersion of the analyte molecules. Here, Δt depends less on the frequency f ($\Delta t \propto 1/\sqrt[3]{f}$, dashed black line) compared to Figure 3a,b since the observed time lag is caused by both advection and diffusion, where the contribution of advection is independent of f (see Supplementary Note 3). Furthermore, diffusion occurs on a length scale smaller than H, reducing its contribution to the frequency dependency. The inset shows the same data visualized as the phase lag $\Delta\phi$ as a function of f. For increasing f, the absolute phase lag increases ($\Delta\phi$ becomes more negative) due to the time needed to transport analyte molecules from the bulk of the measurement chamber to the sensor surface. For large f, $C_a(t)$ can lag for multiple cycles with respect to $C_{a,0}(t)$ (not shown here), though ΔC_a decreases sharply due to dispersion for $f > f_c^A$ (see top graph).

Figure 4b visualizes cutoff frequency f_c as a function of flow rate Q measured at two positions, namely, in the bulk of the measurement chamber (position 1, dark brown line) and at the

https://doi.org/10.1021/acssensors.1c02307
ACS Sens. 2022, 7, 286−295

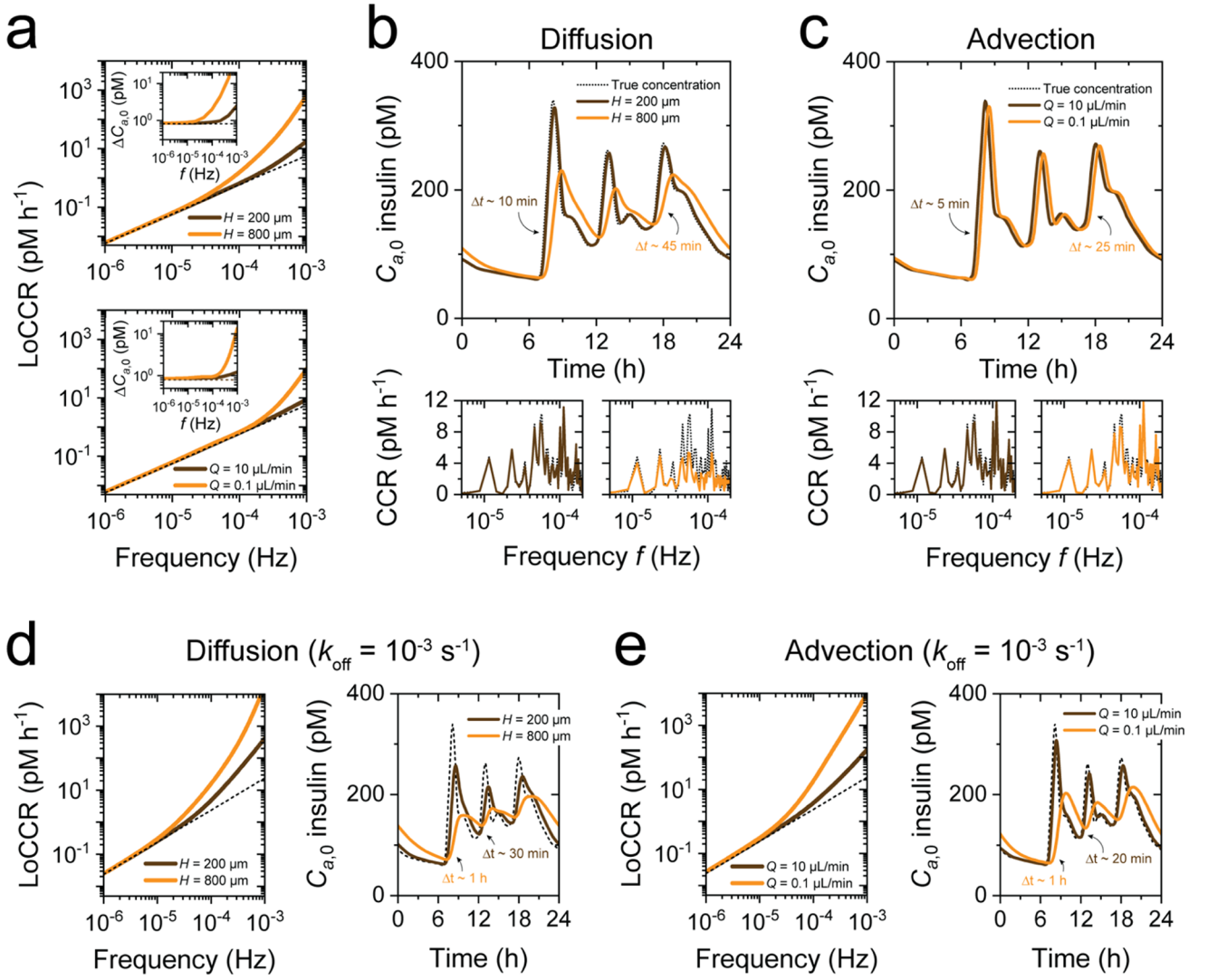

Figure 5. Measuring concentration-time profiles using two modes of continuous analyte exchange. (a) Limit of quantification of CCR (LoCCR) as a function of frequency f in a monitoring system with continuous analyte exchange by diffusion-based sampling (top) and by advection-based sampling (bottom). The insets show the same data with the concentration change $\Delta C_{a,0}$ as a function of f. For a low f, the precision of the CCR is limited by Poisson noise (dashed black line). For increasing f, the lines start to deviate since the frequencies become higher than the corresponding cutoff frequencies. (b) Concentration-time profiles for a measurement chamber height H = 200 μm (brown line) and H = 800 μm (orange line), and the true analyte concentration (black dotted line), for diffusion-based analyte exchange. The bottom graphs show the frequency spectrum with the CCR component as a function of frequency. For a small H, the concentration-time profile closely resembles the true concentration-time profiles. However, for a large H, the similarity is only visible at low frequencies; at high frequencies, the measured CCR is close to 0, indicating that sinusoidal components with these frequencies are not present in the measured signal. (c) Concentration-time profiles for a measurement chamber with flow rate Q = 10 μL/min (brown line) and Q = 0.1 μL/min (orange line), and the true analyte concentration (black dotted line, behind the brown line), for advection-based analyte exchange. The bottom shows the frequency spectrum. For both flow rates, the concentration-time profile closely resembles the true concentration-time profile. (d, e) LoCCR as a function of f and the corresponding concentration-time profiles for diffusion-based analyte exchange (d) and advection-based analyte exchange (e), where k_{off} = 10^{-3} s^{-1} (compared to k_{off} = 10^{-2} s^{-1} in panels (a) and (b), see Table 1). Due to higher cutoff frequencies, the similarity of the measured concentration-time profiles is less compared to panels (b) and (c).

surface of the measurement chamber (position 2, orange line). The black arrow indicates the standard parameter value for Q as listed in Table 1. The inset shows the same data with f_c (normalized to τ_A) as a function of Pe_L. For a small Q, there is a concentration gradient in the longitudinal direction since the distance over which molecules need to diffuse to the sensor surface is smaller compared to the situation in Figure 3. This results in an advection-limiting process at Pe_L < 1 with a constant f_c. For increasing Q, the observed f_c becomes different when measuring in the bulk or at the sensor surface. For measuring in the bulk, an increased Q results in a change of the shape of the concentration gradient, namely, perpendicular to the velocity profile (top sketch, dashed black profile) instead of in the longitudinal direction. The flow rate where f_c becomes advection-limited depends on the measurement chamber geometry: for a small L, f_c is advection-limited at small flow rates since the distance over which molecules need to be transported is small. For measuring at the sensor surface, the stationary layer becomes smaller for increasing Q effectively decreasing the distance over which the molecules need to diffuse to the sensor surface. This effect results in f_c scaling with the advection time less than $1/\tau_A$ (see the main graph,

https://doi.org/10.1021/acssensors.1c02307
ACS Sens. 2022, 7, 286−295

dashed black lines) and that the normalized cutoff frequency f_c decreases (see inset).

Figure 4c visualizes the cutoff frequency f_c as a function of the flow rate Q (top) and the mean analyte concentration $C_{a,0}$ in the system of interest (bottom), where diffusion, advection, and reaction are included. Standard values for the flow rate Q and mean concentration $C_{a,0}$ are indicated by the black arrows (see Table 1). In the top graph, for a low Q, the cutoff frequency is advection-limited, where $f_c = f_c^A \sim 1/\tau_A$. For a large Q, the cutoff frequency is limited by a combination of diffusion and reaction. The inset shows the same data with f_c (normalized to the advection time τ_A) as a function of Pe_L. In the bottom graph, for a low $C_{a,0}$, the reaction is slow, which causes the observed cutoff frequency f_c to be dissociation rate-limited, where $f_c = f_c^R \sim k_{off}$. For a large $C_{a,0}$, the reaction is association rate-limited, where $f_c = f_c^R \sim k_{on}C_{a,0}$. The inset shows the same data with f_c (normalized to the diffusion time τ_D) as a function of the Damköhler number Da. For a small Da, the cutoff frequency is reaction-limited (dashed black line). For a large Da, the cutoff frequency becomes diffusion-limited.

Continuous Biomolecular Monitoring for Arbitrary Concentration Profiles. The measured concentration profile of a monitoring sensor should resemble as closely as possible the true concentration profile of the analyte. While Figures 3 and 4 discussed the effects of diffusion, advection, and reaction on the cutoff frequency and lag time, the question remains how these processes influence an actual concentration profile and the differences between the measured and the true concentration profiles. Here, we study an insulin concentration profile with standard parameter values listed in Table 1 as an example (see Supplementary Note 6). In this paper, the rate sensitivity is quantified as the limit of quantification of CCR (LoCCR), *i.e.*, the smallest CCR that can be measured with an error of 10% (see Supplementary Note 5). The LoCCR is calculated assuming a sensor with noise that is dominated by Poisson statistics, with a signal collection area $A_s = 1$ mm^2, and a binder density $\Gamma_b = 10^{-9}$ mol m^{-2}. Poisson noise represents the fundamental limit of the precision that can be achieved in a biosensor due to stochastic fluctuations in the number of detected analyte molecules.[28,29]

Figure 5 shows the collective influence of diffusion, advection, and reaction on LoCCR and the measured concentration profile, for different measurement chamber heights H (in the case of diffusion-based analyte exchange) and for different flow rates Q (in the case of advection-based analyte exchange). Figure 5a shows LoCCR as a function of frequency f, for diffusion-based sampling (top) and advection-based sampling (bottom). The top graph shows results for measurement chamber heights $H = 200$ μm (dark brown) and $H = 800$ μm (orange). For a low f, LoCCR equals the value found for Poisson noise only (dashed black line, see also Supplementary Note 5), which is due to the fact that the sensor reaches equilibrium and no dispersion occurs (*cf.* Figure 3). For increasing f, the results depend on the measurement chamber height because a small H gives a larger cutoff frequency (see Figure 3c). Here, both lines deviate from the Poisson limit since equilibrium is not reached within a time equal to $1/f$, resulting in fewer analyte−binder complexes. The inset shows the same data with the minimum concentration change $\Delta C_{a,0}$ that can be quantified with an error of less than 10% as a function of frequency f. The bottom graph shows advection-based sampling with flow rates $Q = 10$ μL/min (dark brown) and $Q = 0.1$ μL/min (orange).[30−32] Here, the lines deviate from the Poisson limit at higher frequencies compared to diffusion-based sampling since the cutoff frequency is higher in advection-based sampling compared to diffusion-based sampling (see Figures 3c and 4c). The inset shows the same data with the minimum concentration change $\Delta C_{a,0}$ that can be quantified with an error of less than 10% as a function of frequency f.

Figure 5b shows a typical insulin profile (dotted black line) and corresponding measured insulin profiles, using diffusion-based analyte exchange and the standard parameter values listed in Table 1. The bottom graphs show the frequency spectrum of the true and measured insulin profiles plotted as CCR components (see Supplementary Note 2). For $H = 200$ μm (brown line), the measured concentration profile is almost identical to the true concentration profile since the cutoff frequency $f_c = 9 \times 10^{-4}$ Hz (see Figure 3c) is higher than the frequencies present in the true insulin profile (see bottom graphs, left). For $H = 800$ μm (orange line), the true concentration profile cannot be accurately reconstructed, only the general up-and-down trend at a 6-hour interval, since the cutoff frequency $f_c = 1 \times 10^{-4}$ Hz (see Figure 3c) is close to the frequencies in the insulin profile (see bottom graphs, right). Also, the average lag time Δt of the measured signal is smaller for $H = 200$ μm than for $H = 800$ μm since a smaller distance requires less time for diffusion.

Figure 5c shows the results for advection-based analyte exchange, for flow rates $Q = 10$ μL/min (dark brown) and $Q = 0.1$ μL/min (orange). In both cases, the measured insulin profile is similar to the true insulin profile since the cutoff frequencies are $f_c = 7 \times 10^{-3}$ Hz and $f_c = 8 \times 10^{-4}$ Hz, respectively (see Figure 4c, top). The strong similarities are also visible in the frequency spectrum (bottom panel).

Figure 5d,e investigates the limits of dynamic monitoring when affinity binders with very high affinity are used, *i.e.*, binders with a very low dissociation rate constant ($k_{off} = 10^{-3}$ s^{-1}), which is relevant to study when low-concentration analytes need to be measured. Figure 5d shows simulation results for diffusion-based sampling. The data show that the lower dissociation rate constant causes a lower cutoff frequency, a longer lag time, and a higher LoCCR (see Supplementary Note 5). The reversibility of the sensor is worse, particularly for a large measurement chamber height ($H = 800$ μm) because the large volume of the measurement chamber contains many analyte molecules. Figure 5e shows results for advection-based sampling. The flow rate increases the rate of exchange of the large volume above the sensor surface. A flow rate as low as 0.1 μL/min already significantly improves the dynamic performance of the sensor. A flow rate of 10 μL/min gives small differences between the measured and real concentrations with a lag time that is very close to $1/k_{off} = 1/(10^{-3}\ s^{-1}) = 17$ min.

CONCLUSIONS

To measure in real time the dynamic changes of biomolecular concentrations in biological systems or biotechnological processes, monitoring sensors are required that reveal reliable concentration−time profiles. We have studied the influence of sensor design parameters on the differences between the true and the measured concentration−time profile, focusing on the lag time of the sensor signal with respect to the input concentration and on the rate sensitivity. To quantify a rate sensitivity, we introduced the concept of concentration change rate (CCR), which is expressed in the units molar per second.

https://doi.org/10.1021/acssensors.1c02307
ACS Sens. 2022, 7, 286−295

The CCR that needs to be resolved differs strongly between different biomolecular monitoring applications, due to their respective concentration changes and fluctuation times. The limit of the measurable concentration change rate was evaluated as the limit of CCR (LoCCR), *i.e.*, the lowest CCR that can be quantified with a precision of 10%.

In this work, we have presented a comprehensive methodology to study the properties and limitations of dynamic measurements using affinity-based sensors, as these represent a very generic and broad class of bioanalytical measurement techniques. Analyte exchange was considered between the system of interest and the sensor by diffusive as well as advective sampling. Finite-element simulations were used to describe the spatial and temporal dependency of analyte concentration within the measurement chamber. Sinusoidal concentration−time profiles were studied as well as arbitrary concentration−time profiles by frequency decomposition. Using this approach, the effects of mass transport and biochemical kinetics on the speed of concentration change, time delays, and concentration errors in the sensing system were studied.

The study of sensor performance was exemplified for insulin monitoring. The results show that diffusion-based sampling performs equal to advection-based sampling in reconstructing the concentration−time profile for small heights of the measurement chamber (<200 μm). However, for larger heights, diffusion-based sampling causes an increased lag time and decreased CCR sensitivity. A monitoring system with advection-based sampling performs similarly with respect to the CCR sensitivity for flow rates down to ∼0.1 μL min^{-1}, while the lag time is larger for low flow rates.

For low concentrations of biomolecules, fewer molecules are available for the detection and therefore continuous monitoring sensors with single-molecule resolution are suitable because these sensors can have Poisson-limited noise levels and therefore a high detection sensitivity. In the case of binder molecules with a high affinity (k_{off} = 10^{-3} s^{-1}), the analytical performance deteriorates for diffusion-based sampling, but not for advection-based sampling with flow rates of 10 μL min^{-1} and higher, allowing the measurement of all CCR components present in an insulin concentration−time profile.

The results and learnings presented in this paper can assist researchers to identify the most important processes influencing the performance of continuous monitoring sensors. As a next step, it will be interesting to compare the simulation results to experimental data, for example, on how concentration−time profiles with different frequency components affect the observed signals. Insights into the individual and combined influence of analyte diffusivity, analyte concentration, binder affinity, sampling method, measurement chamber geometry, and flow speed on the observed lag time and rate sensitivity of the measured concentration−time profile will help researchers to develop monitoring systems with desirable sensor characteristics for a diverse range of biomarkers and applications.

■ ASSOCIATED CONTENT

Supporting Information

The Supporting Information is available free of charge at https://pubs.acs.org/doi/10.1021/acssensors.1c02307.

Finite-element simulations, CCR quantification, algebraic derivations of dependencies, equations and precisions, and example calculations of insulin monitoring (PDF)

■ AUTHOR INFORMATION

Corresponding Author

Menno W. J. Prins − *Department of Biomedical Engineering, Eindhoven University of Technology, Eindhoven 5612 AZ, the Netherlands; Department of Applied Physics, Eindhoven University of Technology, Eindhoven 5612 AZ, the Netherlands; Institute for Complex Molecular Systems (ICMS), Eindhoven University of Technology, Eindhoven 5612 AZ, the Netherlands; Helia Biomonitoring, Eindhoven 5612 AZ, the Netherlands;* orcid.org/0000-0002-9788-7298; Email: m.w.j.prins@tue.nl

Authors

Rafiq M. Lubken − *Department of Biomedical Engineering, Eindhoven University of Technology, Eindhoven 5612 AZ, the Netherlands; Institute for Complex Molecular Systems (ICMS), Eindhoven University of Technology, Eindhoven 5612 AZ, the Netherlands;* orcid.org/0000-0001-7554-1141

Arthur M. de Jong − *Department of Applied Physics, Eindhoven University of Technology, Eindhoven 5612 AZ, the Netherlands; Institute for Complex Molecular Systems (ICMS), Eindhoven University of Technology, Eindhoven 5612 AZ, the Netherlands;* orcid.org/0000-0001-6019-7333

Complete contact information is available at: https://pubs.acs.org/10.1021/acssensors.1c02307

Author Contributions

All authors conceived and designed the methodology. R.M.L. conceived, designed, and performed the simulations and the data analysis. All authors interpreted data, discussed results, and co-wrote the paper. All authors approved the submitted version of the manuscript.

Notes

The authors declare the following competing financial interest(s): M.W.J.P. is cofounder of Helia Biomonitoring. All authors declare no further competing interests.

All data supporting the findings of this study are available from the corresponding author upon reasonable request.

All data analysis and simulation codes used for this study are available from the corresponding author upon reasonable request.

■ ACKNOWLEDGMENTS

Part of this work was funded by the Safe-N-Medtech H2020 project under grant agreement number 814607.

■ REFERENCES

(1) Buszko, M.; Nita-Lazar, A.; Park, J.-H.; Schwartzberg, P. L.; Verthelyi, D.; Young, H. A.; Rosenberg, A. S. Lessons Learned: New Insights on the Role of Cytokines in COVID-19. *Nat. Immunol.* **2021**, *22*, 404−411.

(2) Fajgenbaum, D. C.; June, C. H. Cytokine Storm. *N. Engl. J. Med.* **2020**, *383*, 2255−2273.

(3) Yiu, H. H.; Graham, A. L.; Stengel, R. F. Dynamics of a Cytokine Storm. *PLoS One* **2012**, *7*, No. e45027.

(4) Duffy, D. Standardized Immunomonitoring: Separating the Signals from the Noise. *Trends Biotechnol.* **2018**, *36*, 1107−1115.

(5) Chen, P.; Huang, N.-T.; Chung, M.-T.; Cornell, T. T.; Kurabayashi, K. Label-Free Cytokine Micro- and Nano-Biosensing Towards Personalized Medicine of Systemic Inflammatory Disorders. *Adv. Drug Delivery Rev.* **2015**, *95*, 90−103.
(6) Young, A. T.; Rivera, K. R.; Erb, P. D.; Daniele, M. A. Monitoring of Microphysiological Systems: Integrating Sensors and Real-Time Data Analysis Toward Autonomous Decision-Making. *ACS Sens.* **2019**, *4*, 1454−1464.
(7) Zhang, Y. S.; Aleman, J.; Shin, S. R.; Kilic, T.; Kim, D.; Shaegh, S.A.M.; Massa, S.; Riahi, R.; Chae, S.; Hu, N.; et al. Multisensor-Integrated Organs-on-Chips Platform for Automated and Continual In Situ Monitoring of Organoid Behaviors. *Proc. Natl. Acad. Sci. U.S.A.* **2017**, *114*, E2293−E2302.
(8) Heikenfeld, J.; Jajack, A.; Feldman, B.; Granger, S. W.; Gaitonde, S.; Begtrup, G.; Katchman, B. A. Accessing Analytes in Biofluids for Peripheral Biochemical Monitoring. *Nat. Biotechnol.* **2019**, *37*, 407−419.
(9) Kim, J.; Campbell, A. S.; Esteban-Fernández de Ávila, B.; Wang, J. Wearable Biosensors for Healthcare Monitoring. *Nat. Biotechnol.* **2019**, *37*, 389−406.
(10) Heikenfeld, J.; Jajack, A.; Rogers, J.; Gutruf, P.; Tian, L.; Pan, T.; Li, R.; Khine, M.; Kim, J.; Wang, J.; et al. Wearable Sensors: Modalities, Challenges, and Prospects. *Lab Chip* **2018**, *18*, 217−248.
(11) Ates, H. C.; Brunauer, A.; von Stetten, F.; Urban, G. A.; Güder, F.; Merkoçi, A.; Früh, S. M.; Dincer, C. Non-Invasive Diagnostics: Integrated Devices for Non-Invasive Diagnostics. *Adv. Funct. Mater.* **2021**, *31*, No. 2170105.
(12) Rodbard, D. Continuous Glucose Monitoring: A Review of Successes, Challenges, and Opportunities. *Diabetes Technol. Ther.* **2016**, *18*, 3−13.
(13) Klonoff, D. C.; Ahn, D.; Drincic, A. Continuous Glucose Monitoring: A Review of the Technology and Clinical Use. *Diabetes Res. Clin. Pract.* **2017**, *133*, 178−192.
(14) Christodouleas, D. C.; Kaur, B.; Chorti, P. From Point-of-Care Testing to eHealth Diagnostic Devices (eDiagnostics). *ACS Cent. Sci.* **2018**, *4*, 1600−1616.
(15) Boughton, C. K.; Hovorka, R. New Closed-Loop Insulin Systems. *Diabetologia* **2021**, *64*, 1007−1015.
(16) Li, J.; Liang, J. Y.; Laken, S. J.; Langer, R.; Traverso, G. Clinical Opportunities for Continuous Biosensing and Closed-Loop Therapies. *Trends Chem.* **2020**, *2*, 319−340.
(17) Rawson, T. M.; O'Hare, D.; Herrero, P.; Sharma, S.; Moore, L.S.P.; Barra, E. D.; Roberts, J. A.; Gordon, A. C.; Hope, W.; Georgiou, P.; et al. Delivering Precision Antimicrobial Therapy through Closed-Loop Control Systems. *J. Antimicrob. Chemother.* **2018**, *73*, 835−843.
(18) Mage, P. L.; Ferguson, B. S.; Maliniak, D.; Ploense, K. L.; Kippin, T. E.; Soh, H. T. A Closed-Loop Control of Circulating Drug Levels in Live Animals. *Nat. Biomed. Eng.* **2017**, *1*, No. 0070.
(19) Chemmalil, L.; Prabhakar, T.; Kuang, J.; West, J.; Tan, Z.; Ehamparanathan, V.; Song, Y.; Xu, J.; Ding, J.; Li, Z. Online/At-Line Measurement, Analysis and Control of Product Titer and Critical Product Quality Attributes (CQAs) During Process Development. *Biotechnol. Bioeng.* **2020**, *117*, 3757−3765.
(20) Wasalathanthri, D. P.; Rehmann, M. S.; Song, Y.; Gu, Y.; Mi, L.; Shao, C.; Chemmalil, L.; Lee, J.; Ghose, S.; Borys, M. C.; et al. Technology Outlook for Real-Time Quality Attribute and Process Parameter Monitoring in Biopharmaceutical Development - A Review. *Biotechnol. Bioeng.* **2020**, *117*, 3182−3198.
(21) Randek, J.; Mandenius, C.-F. On-Line Soft Sensing in Upstream Bioprocessing. *Crit. Rev. Biotechnol.* **2018**, *38*, 106−121.
(22) Squires, T. M.; Messinger, R. J.; Manalis, S. R. Making It Stick: Convection, Reaction and Diffusion in Surface-Based Biosensors. *Nat. Biotechnol.* **2008**, *26*, 417−426.
(23) Atkins, P.; Paula, De. *Physical Chemistry for the Life Sciences*; Oxford University Press, 2006.
(24) Pundir, C. S.; Kumar, P.; Jaiwal, R. Biosensing Methods for Determination of Creatinine: A Review. *Biosens. Bioelectron.* **2019**, *126*, 707−724.
(25) Yeh, H.-C.; Lo, Y.-C.; Ting, I.-W.; Chu, P.-L.; Chang, S.-N.; Chiang, H.-Y.; Kuo, C.-C. 24-hour Serum Creatinine Variation Associates with Short- and Long-Term All-Cause Mortality: A Real-World Insight into Early Detection of Acute Kidney Injury. *Sci. Rep.* **2020**, *10*, No. 6552.
(26) Meisner, M. Update on Procalcitonin Measurements. *Ann. Lab. Med.* **2014**, *34*, 263−273.
(27) Teachey, D. T.; Lacey, S. F.; Shaw, P. A.; Melenhorst, J. J.; Maude, S. L.; Frey, N.; Pequignot, E.; Gonzalez, V. E.; Chen, F.; Finklestein, J.; et al. Identification of Predictive Biomarkers for Cytokine Release Syndrome after Chimeric Antigen Receptor T-Cell Therapy for Acute Lymphoblastic Leukemia. *Cancer Discovery* **2016**, *6*, 664−679.
(28) Lubken, R. M.; de Jong, A. M.; Prins, M.W.J. How Reactivity Variability of Biofunctionalized Particles Is Determined by Superpositional Heterogeneities. *ACS Nano* **2021**, *15*, 1331−1341.
(29) Lubken, R. M.; Bergkamp, M. H.; de Jong, A. M.; Prins, M.W.J. Sensor for the Rapid Monitoring of Biomolecules at Low Concentrations Over Long Time Spans. *ACS Sensors* **2021**, *6*, 4471−4481.
(30) Nightingale, A. M.; Leong, C. L.; Burnish, R. A.; Hassan, S.; Zhang, Y.; Clough, G. F.; Boutelle, M. G.; Voegeli, D.; Niu, X. Monitoring Biomolecule Concentrations in Tissue Using a Wearable Droplet Microfluidic-Based Sensor. *Nat. Commun.* **2019**, *10*, No. 2741.
(31) Gowers, S. A. N.; Rogers, M. L.; Booth, M. A.; Leong, C. L.; Samper, I. C.; Phairatana, T.; Jewell, S. L.; Pahl, C.; Strong, A. J.; Boutelle, M. G. Clinical Translation of Microfluidic Sensor Devices: Focus on Calibration and Analytical Robustness. *Lab Chip* **2019**, *19*, 2537−2548.
(32) Nandi, P.; Lunte, S. M. Recent Trends in Microdialysis Sampling Integrated with Conventional and Microanalytical Systems for Monitoring Biological Events: A Review. *Anal. Chim. Acta* **2009**, *651*, 1−14.

https://doi.org/10.1021/acssensors.1c02307
ACS Sens. 2022, 7, 286−295